Inorganic Chemistry

pubs.acs.org/IC

Article

Pressure-Induced Structural Phase Transition and Metallization of $CrCl_3$ under Different Hydrostatic Environments up to 50.0 GPa

Meiling Hong, Lidong Dai,* Haiying Hu,* Xinyu Zhang, Chuang Li, and Yu He

Cite This: *Inorg. Chem.* 2022, 61, 4852−4864

Read Online

ACCESS | Metrics & More | Article Recommendations | Supporting Information

ABSTRACT: High-pressure structural, vibrational, and electrical transport properties of $CrCl_3$ were investigated by means of Raman spectroscopy, electrical conductivity, and high-resolution transmission electron microscopy under different hydrostatic environments using the diamond anvil cell in conjunction with the first-principles theoretical calculations up to 50.0 GPa. The isostructural phase transition of $CrCl_3$ occurred at 9.9 GPa under nonhydrostatic conditions. As pressure was increased up to 29.8 GPa, $CrCl_3$ underwent an electronic topological transition accompanied by a metallization transformation due to the discontinuities in the Raman scattering and electrical conductivity, which is possibly belonging to a typical first-order metallization phase transition as deduced from first-principles theoretical calculations. As for the hydrostatic condition, a ∼2.0 GPa pressure delay in the occurrence of two corresponding transformations of $CrCl_3$ was observed owing to the different deviatoric stress. Upon decompression, we found that the phase transformation from the metal to semiconductor in $CrCl_3$ is of good reversibility, and the obvious pressure hysteresis effect is observed under different hydrostatic environments. All of the obtained results on the structural, vibrational, and electrical transport characterizations of $CrCl_3$ under high pressure can provide a new insight into the high-pressure behaviors of representative chromium trihalides CrX_3 (X = Br and I) under different hydrostatic environments.

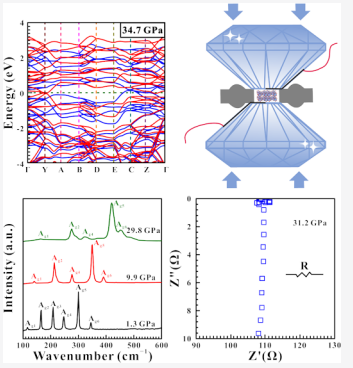

1. INTRODUCTION

In recent years, chromium trihalides CrX_3 (X = Cl, Br, I), a type of binary semiconductors belonging to the VI−VII group compounds, have motivated intense studies in the fields of heterostructures, spintronic devices, and sensing nanodevices owing to their peculiar electronic and magnetic properties.[1,2] Among CrX_3 semiconductors, $CrCl_3$ is the most stable compound with a monoclinic crystal symmetry and space group of $C2/m$ under ambient conditions.[3] The $C2/m$ phase of $CrCl_3$ is of a two-dimensional layered structure, where each chromium atom is coordinated by six neighboring chlorine atoms to constitute edge-shared octahedra in a monolayer, and the layers are stacked along the *c*-axis direction through the weak van der Waals interlayer forces.[1,2]

As usual, pressure is one of the most important influential factors of regulating the lattice vibration and electrical transport properties for some layered metallic compounds (e.g., MoS_2, $MoSe_2$, $MoTe_2$, ReS_2, As_2S_3, As_2Te_3, Sb_2S_3, $CrCl_3$, etc.).[4−17] As a representative transition-metal trihalide, $CrCl_3$ has rarely been studied under high pressure. To our knowledge, only one high-pressure investigation on the structural, magnetic, and electronic properties of $CrCl_3$ has been performed by Ahmad et al. (2020) up to 40.9 GPa in a diamond anvil cell (DAC) under different hydrostatic environments by virtue of synchrotron X-ray diffraction (XRD), Raman spectroscopy, photoluminescence spectroscopy measurements, and first-principles theoretical calculations.[17] Their synchrotron XRD and Raman scattering results for $CrCl_3$ revealed an isostructural phase transition (IPT) at 11.0 GPa based on the discontinuities in volume and axial ratios, the mergence of M2 and M3 Raman peaks, the inflection points in the Raman shift, spacings in the Raman shift, and Raman full width at half-maximum (fwhm). Further, the photoluminescence spectroscopy and first-principles theoretical calculations results confirmed that the IPT belongs to a semiconductor-to-semiconductor phase transition, which is accompanied by a magnetic transformation from the ferromagnetic to antiferromagnetic phases. Upon further compression above 28.0 GPa, an electronic topological transition (ETT) was identified from the redshift of the M1 Raman mode and the significant broadening of Raman peaks. Notably, they acquired similar pressure points of phase transitions under different hydrostatic environments, which is probably caused by the inevitably pressure-induced solidification of silicone oil around 3.0 GPa.[18] On the other hand, it is well known that the hydrostaticity of the sample chamber of DAC plays a vital role in exploring the pressure-induced structural transition for some layered metallic compounds (e.g., MoS_2, $MoSe_2$, $MoTe_2$, ReS_2, As_2Te_3, etc.).[4,6,8,10,13] In comparison with the lower solid-

Received: November 8, 2021
Published: March 15, 2022

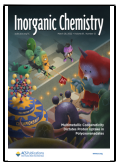

https://doi.org/10.1021/acs.inorgchem.1c03486
Inorg. Chem. 2022, 61, 4852−4864

ification pressure point of silicone oil, some representative noble gases (e.g., helium, neon, etc.) have been considered as a better pressure medium due to their stable physicochemical properties and high hydrostaticity, which have been widely applied to various material physical characterizations under high temperature and high pressure in the DAC.[5,6,8,12,15,19] As far as $CrCl_3$ is concerned, systematic research is crucial for exploring the influence of hydrostaticity on the phase transition pressure points under different hydrostatic environments. Besides, it is generally accepted that high-pressure electrical conductivity and Raman scattering measurements are efficient methods in disclosing the occurrences of the IPT and ETT for some metallic compounds.[15,16,20−23] Until now, there is no related report on high-pressure electrical conductivity data of chromium trihalides.

In the present study, we reported an isostructural phase transition and a semiconductor-to-metal transformation for $CrCl_3$ under nonhydrostatic and hydrostatic environments up to 50.0 GPa in a DAC combined with Raman spectroscopy, alternating current (AC) impedance spectroscopy, high-resolution transmission electron microscopy (HRTEM), and first-principles theoretical calculations. Furthermore, the observed pressure-induced phase transitions of $CrCl_3$ were discussed under compression and decompression processes in detail.

2. EXPERIMENTAL DETAILS

2.1. Sample Preparation and Characterization. High-purity (99.9%) $CrCl_3$ powder with a purple surface color (see the inset in Figure 1) was purchased from Alfa Aesar as the starting samples for high-pressure Raman scattering and electrical conductivity measurements. We determined the crystalline structure of the initial sample using the XRD analysis using an Empyrean-type X-ray powder diffractometer with the diffraction angle ranging from 10 to 70°. The lattice parameters of the starting sample were acquired by fitting the XRD pattern with MDI Jade 6.5 software. A typical XRD pattern for the starting sample is displayed in Figure 1, which demonstrates that the sample initially has a monoclinic structure with the space group of $C2/m$ (JCPDS no. 73-0309). The corresponding lattice parameters for the initial sample were listed as follows: a = 5.9617 Å, b = 10.3361 Å, c = 6.1244 Å, $\alpha = \gamma = 90.0°$, $\beta = 108.6°$, and V = 357.7 Å^3, which match well with prior results.[2,24]

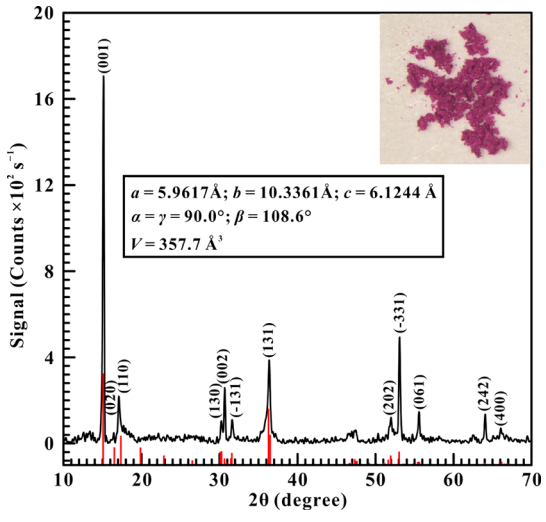

Figure 1. Representative XRD pattern of the starting sample. Here, the red vertical lines represent the standardized peak positions of the monoclinic structure of $CrCl_3$. Major peaks of the initial sample are marked by (hkl) indices. Inset: optical microscope photograph and the corresponding lattice parameters for the initial sample.

2.2. High-Pressure Raman Spectroscopy Experiments. A symmetric DAC with a culet diameter of 300 μm and bevel angle of 10° was employed for in situ Raman scattering and electrical conductivity experiments. A 250 μm thick T-301 stainless steel gasket was preindented into ∼40 μm in thickness. Successively, we manufactured a centrical hole, having a diameter of 100 μm with a laser drilling machine, which acted as the sample chamber. The sample along with a ruby sphere, serving as pressure calibration, was loaded into the sample chamber. Two sets of independent Raman spectroscopy experiments were implemented under different hydrostatic environments, without pressure medium for the nonhydrostatic condition and helium as the pressure medium for the hydrostatic condition, respectively. We investigated the high-pressure Raman spectra of $CrCl_3$ using a Renishaw 2000 microconfocal Raman spectrometer coupled with a 514.5 nm argon ionic excitation source. Single-crystal silicon with a characteristic Raman peak at 520.0 cm^{-1} was utilized to calibrate the Raman spectroscopy system prior to measurement. Raman spectra of $CrCl_3$ were gathered within the wavenumber range of 100−600 cm^{-1} in the backscattering geometry with the spectral resolution of 1.0 cm^{-1} and exposure time of 120 s, respectively. The pressure equilibrium within the sample chamber was realized by waiting 15 min between each measurement. We processed the obtained Raman spectra with a Lorentzian-type function in Origin 8.5 software to extract the Raman peak position and its corresponding fwhm.

2.3. High-Pressure Electrical Conductivity Experiments. In our high-pressure electrical conductivity experiment of $CrCl_3$, a clean T-301 stainless steel gasket was firstly preindented to ∼60 μm, and then a 180 μm centrical hole was drilled into the indentation. We pressurized the insulating powder composed of boron nitride and epoxy into the hole, and another hole having a diameter of 100 μm was fabricated as the insulation sample chamber. The remaining part of the gasket was covered by the insulating cement. For the sake of avoiding the introduction of additional errors, a no-pressure medium was applied in our electrical conductivity measurements. We measured the impedance spectra of $CrCl_3$ through a Solartron-1260 impedance/gain phase analyzer within the frequency range of 10^{-1} to 10^7 Hz and at a signal voltage of 1.0 V. During variable-temperature electrical conductivity measurements, a low-temperature condition was produced by the refrigeration of liquid nitrogen, and the temperature was monitored through a standard k-type thermocouple adhered to the side face of the diamond. More details of the high-pressure experimental technique and measurement procedures have been published previously.[4,15,25]

2.4. HRTEM Observation. Microscopical structural characterizations for the starting and recovered samples decompressed under nonhydrostatic and hydrostatic environments were investigated using HRTEM, which was operated at the State Key Laboratory of Environmental Geochemistry, Institute of Geochemistry, Chinese Academy of Sciences, Guiyang, China. A small amount of sample was homogeneously distributed onto a carbon-film-coated copper grid for the HRTEM observation, which was performed through a Tecnai G2 F20 S-TWIN TMP with an acceleration voltage of 200 kV. We precisely measured the interplanar spacings of the samples through Digital Micrograph software.

2.5. First-Principles Theoretical Calculations. First-principles theoretical calculations on $CrCl_3$ were conducted using the Vienna Ab Initio Simulation Package (VASP) based on density functional theory (DFT) over a wide pressure range from 0 to 50.0 GPa at the Hefei Advanced Computing Center of China.[26,27] The electron−ion interactions are represented by the projector augmented wave (PAW) scheme within the generalized gradient approximation (GGA).[28,29] In order to realize much higher calculating accuracy and precision, the cut-off energy of 800 eV and the Monkhorst−Pack k meshes with a grid spacing of approximately 0.03 Å^{-1} were adopted in the theoretical calculations. The electronic structure of $CrCl_3$ was optimized at each corresponding pressure point until all the forces acting on ions were less than 0.01 eV/Å per atom at the pressure range from 0 to 50.0 GPa. The enthalpies were calculated on the basis of the

https://doi.org/10.1021/acs.inorgchem.1c03486
Inorg. Chem. 2022, 61, 4852−4864

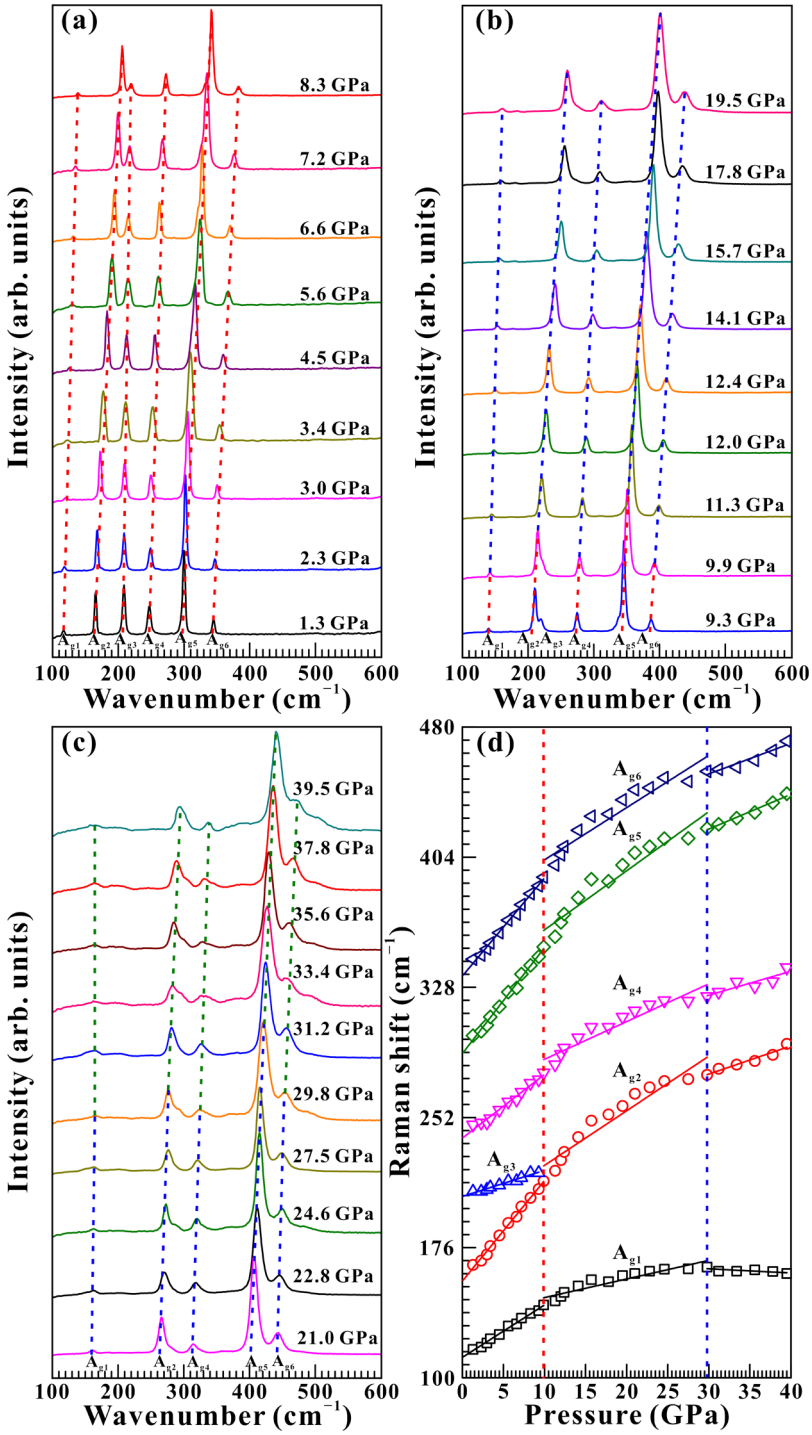

Figure 2. (a–c) Raman spectra of $CrCl_3$ under conditions of 1.3–39.5 GPa within the wavenumber range of 100–600 cm^{-1} upon compression. (d) Corresponding pressure dependence of the Raman shift for $CrCl_3$ under nonhydrostatic conditions. Errors in Raman wavenumber are within the size of the symbol.

optimized free energy, pressure, and volumes. On the one hand, a series of calculated parameters characteristic of the crystalline constants, including the pressure-dependent unit cell volume, lattice constant, angle, lattice constant ratio, and normalized lattice constant, were successfully obtained over a wide pressure range from 0 to 50.0 GPa. On the other hand, a series of calculated parameters characteristic of the electronic structures, including the pressure-dependent band gap energy and density of state (DOS), were obtained at three representative pressure points of 0, 17.9, and 34.7 GPa, respectively. Besides, in order to further check the possible existence of the strong correlation behavior of chromium electrons at high pressure, two different U values (U = 0.0 eV and U = 3.0 eV) of the Hubbard-type correction were selected in the electronic structure calculations at a fixed pressure of 34.7 GPa.[30,31] For more detailed calculation methods and procedures for the first-principles theoretical calculations, please refer to our recently reported results.[32−36]

3. RESULTS AND DISCUSSION

3.1. High-Pressure Raman Spectroscopy Results. Raman spectroscopy is a powerful method of probing subtle changes in lattice vibration and thus has been extensively

https://doi.org/10.1021/acs.inorgchem.1c03486
Inorg. Chem. 2022, 61, 4852−4864

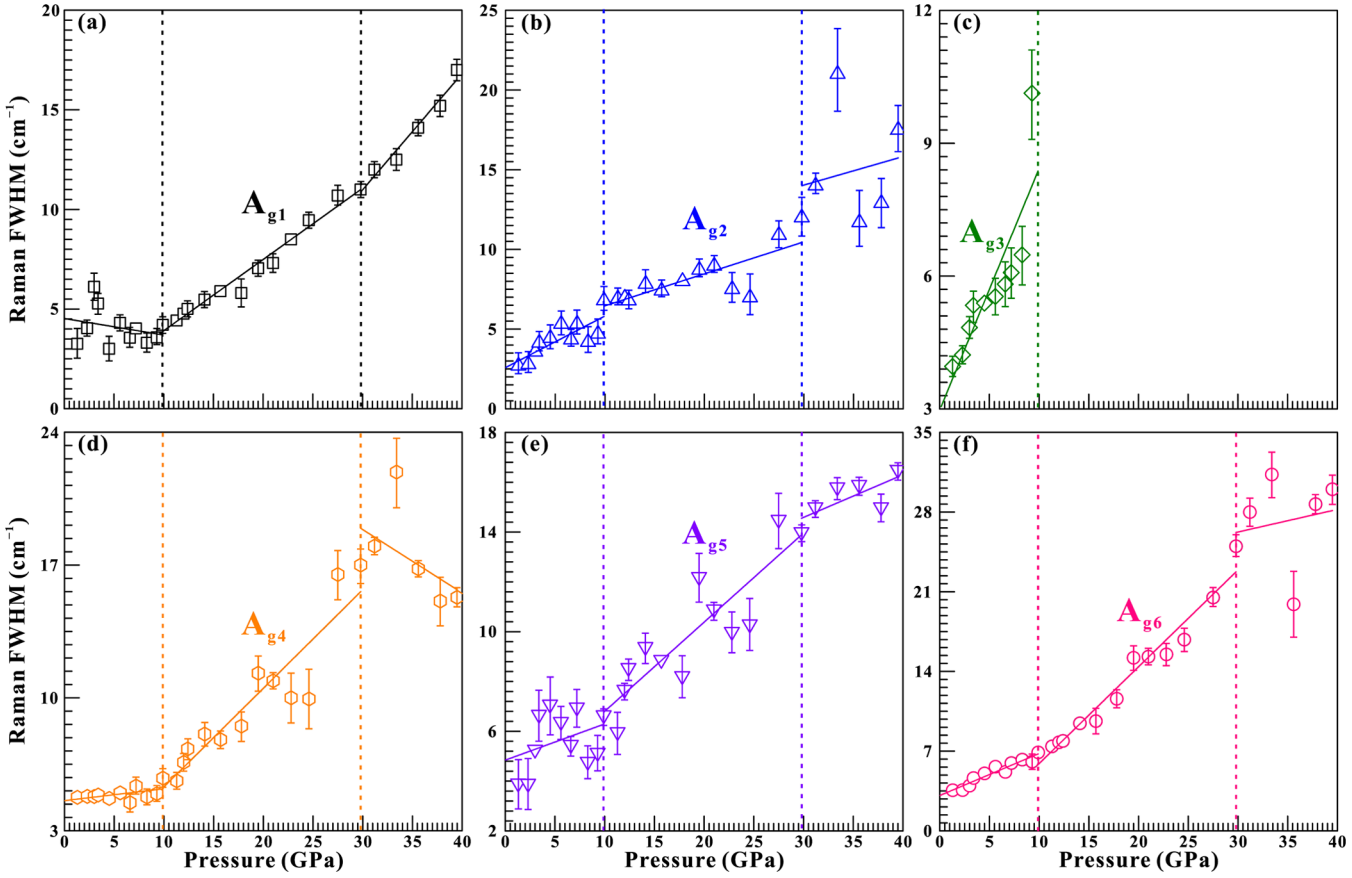

Figure 3. Evolution of Raman fwhm of (a) A_{g1}, (b) A_{g2}, (c) A_{g3}, (d) A_{g4}, (e) A_{g5}, and (f) A_{g6} with pressure for $CrCl_3$ under nonhydrostatic conditions.

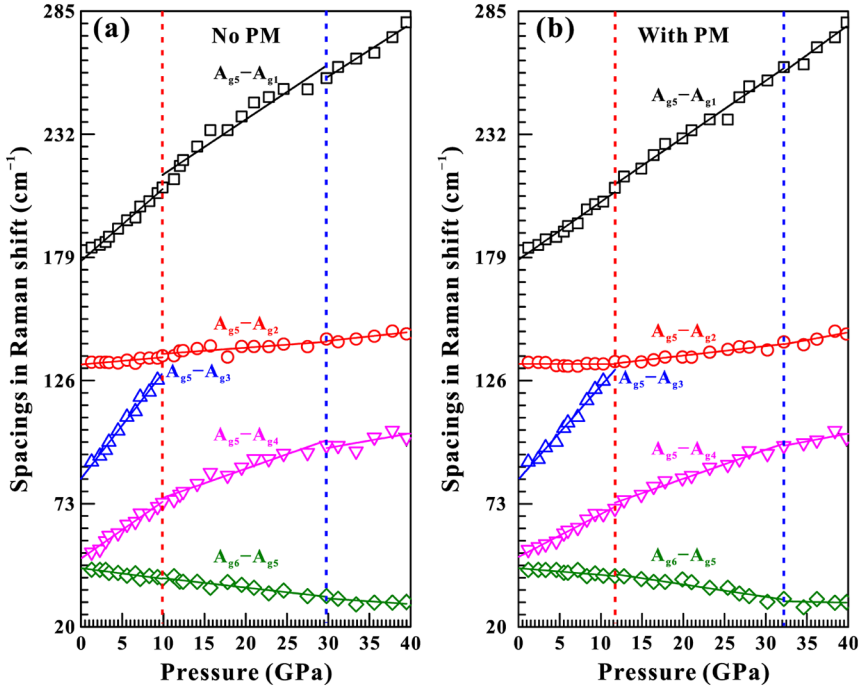

Figure 4. Pressure-dependent spacings in the Raman shift for $CrCl_3$. Here, (a) nonhydrostatic conditions, (b) hydrostatic conditions, respectively. The signal of PM represents the pressure medium. Errors in spacings in the Raman shift are within the size of the symbol.

adopted to investigate structural phase transitions of layered metallic compounds.[4−6,8,10−16] Figure 2a−c show the high-pressure Raman spectra for $CrCl_3$ within the pressure range of 1.3−39.5 GPa under nonhydrostatic conditions. The Raman shift of $CrCl_3$ under high pressure and the corresponding fitting results are displayed in detail in Figure 2d and Table S1,

https://doi.org/10.1021/acs.inorgchem.1c03486
Inorg. Chem. 2022, 61, 4852−4864

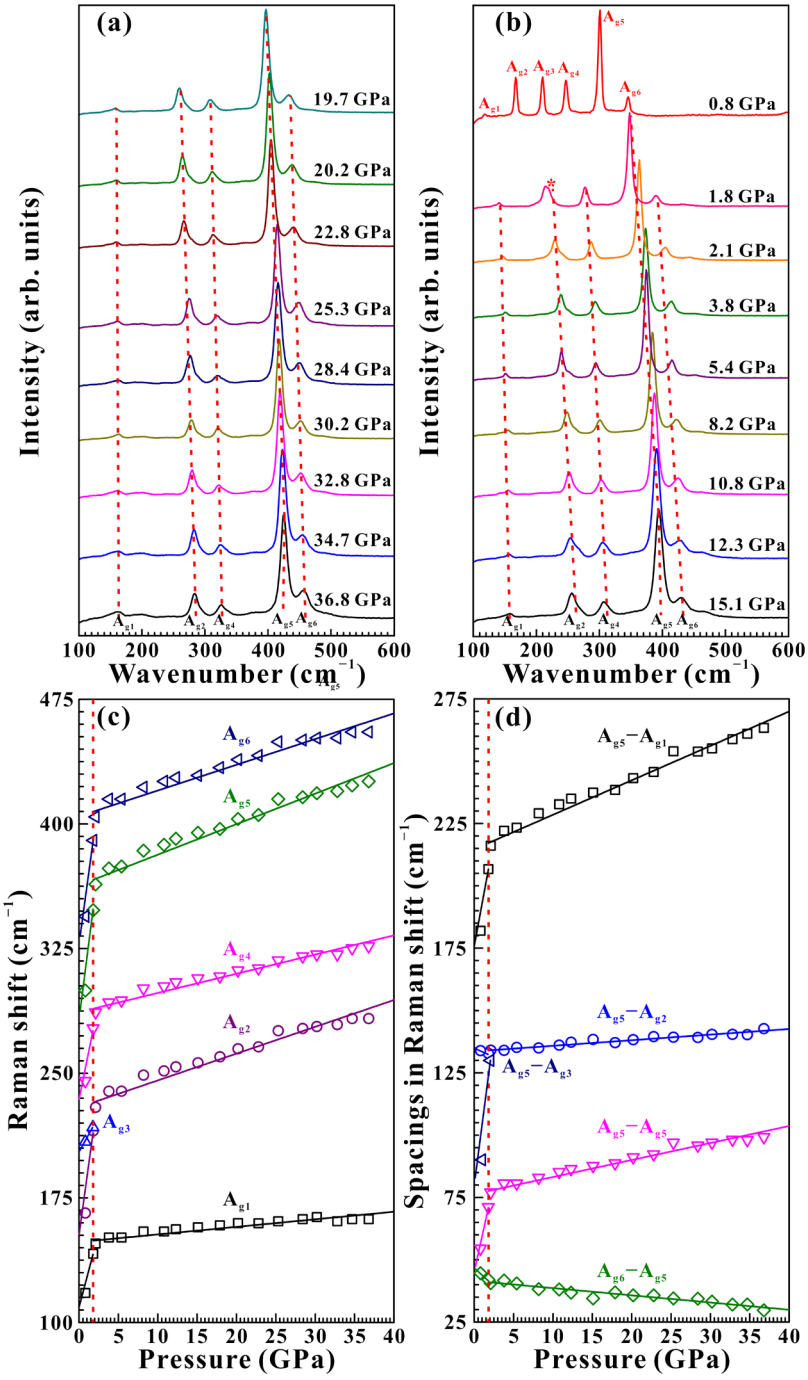

Figure 5. (a,b) High-pressure Raman spectra of $CrCl_3$ within the pressure range of 36.8−0.8 GPa upon decompression. The peak marked by an asterisk indicated the emergence of the A_{g3} Raman peak. Corresponding evolution of (c) Raman shift and (d) spacings in Raman shift as a function of pressure under nonhydrostatic conditions, respectively. Errors in Raman wavenumber and spacings in Raman shift are within the size of the symbol.

respectively. As illustrated in Figure 2a, six representative Raman peaks at 116.6, 165.9, 208.8, 247.7, 299.8, and 344.4 cm^{-1} were observed within the wavenumber range of 100−600 cm^{-1} at a pressure of 1.3 GPa, which can be attributed to the A_g mode deriving from the intralayer vibration.[37,38] To effectively distinguish these Raman peaks, we defined the Raman peaks at 116.6, 165.9, 208.8, 247.7, 299.8, and 344.4 cm^{-1} as the A_{g1}, A_{g2}, A_{g3}, A_{g4}, A_{g5}, and A_{g6} modes of $CrCl_3$, respectively. Moreover, all of these Raman peaks for $CrCl_3$ agree well with previous results.[2,17,37−39]

As seen from Figure 2a−c, the A_{g1}, A_{g2}, A_{g3}, A_{g4}, A_{g5}, and A_{g6} modes of $CrCl_3$ shifted toward higher wavenumbers as the pressure raised with greater rates of 3.06, 5.88, 1.52, 3.72, 6.18, and 5.73 cm^{-1} GPa^{-1} up to 9.9 GPa. Simultaneously, the Raman peak intensity of A_{g3} diminished remarkably with enhancing pressure, and further, the A_{g3} peak disappeared when the pressure reached 9.9 GPa. Within the pressure range of 9.9−29.8 GPa, the A_{g1}, A_{g2}, A_{g4}, A_{g5}, and A_{g6} modes exhibited gentle blueshifts with the application of pressure at the speeds of 1.09, 3.18, 2.20, 3.45, and 3.04 cm^{-1} GPa^{-1}, respectively. The vanishing of the A_{g3} Raman peak and the evident inflection point

https://doi.org/10.1021/acs.inorgchem.1c03486
Inorg. Chem. 2022, 61, 4852−4864

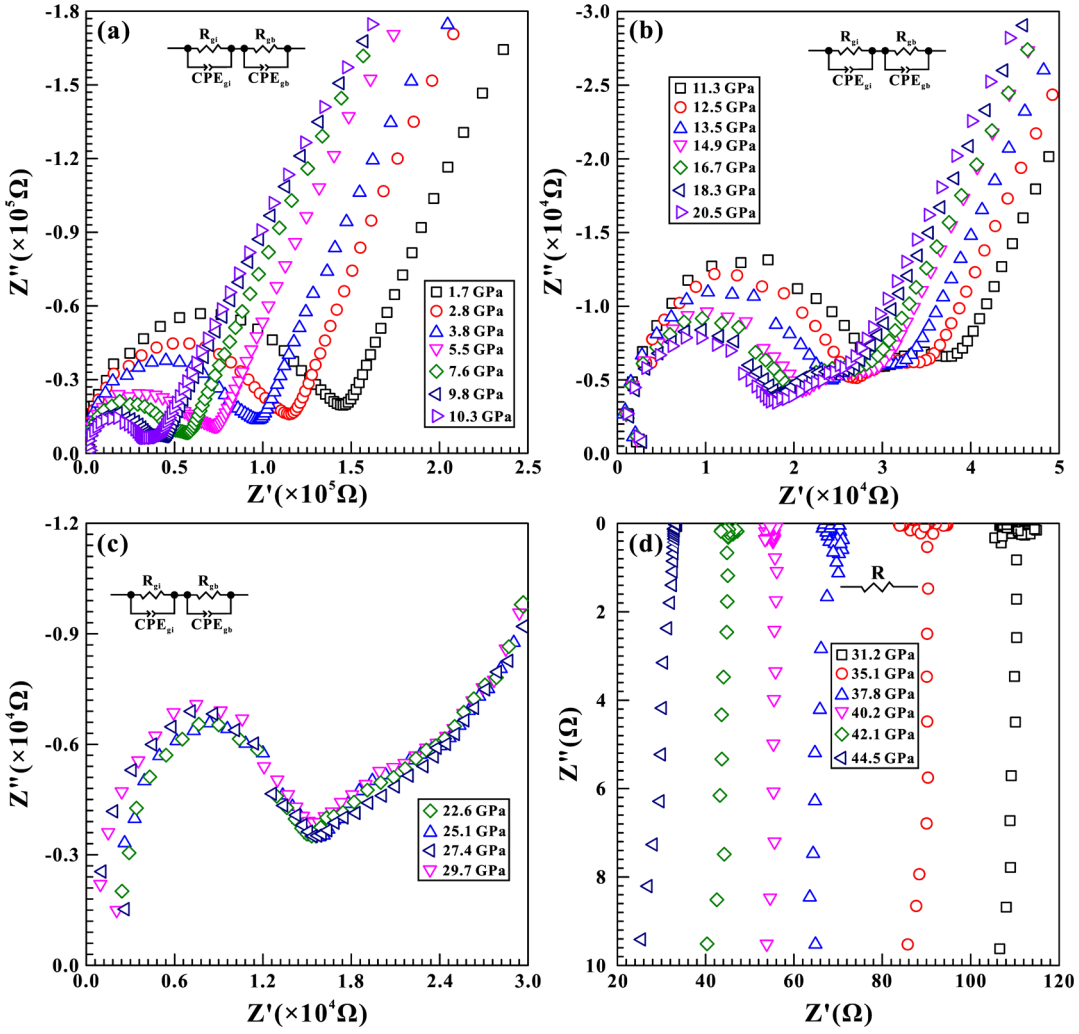

Figure 6. Representative complex impedance spectra of $CrCl_3$ within the pressure ranges from 1.7 to 44.5 GPa. Here, (a) 1.7−10.3, (b) 11.3−20.5, (c) 22.6−29.7, and (d) 31.2−44.5 GPa, respectively. Within the pressure range of 1.7−29.7 GPa, an equivalent circuit of R/CPE was established in parallel to fit these impedance arcs (R_{gi} and R_{gb} are the resistances of the grain interior and grain boundary, respectively; CPE_{gi} and CPE_{gb} represent the constant phase elements of the grain interior and grain boundary, respectively). Above 31.2 GPa, a simple resistance (R) was employed to fit the oblique line in the fourth quadrant. The signals of Z' and Z'' stand for the real and imaginary parts of the complex impedance, respectively.

in the pressure-dependent Raman shift confirm the occurrence of the IPT in $CrCl_3$ at 9.9 GPa. Above 29.8 Gpa, the A_{g1} mode displayed a redshift at a rate of −0.24 cm^{-1} Gpa^{-1}, and the remaining Raman modes of A_{g2}, A_{g4}, A_{g5}, and A_{g6} monotonically shifted toward higher wavenumbers with smaller rates of 1.64, 1.40, 2.02, and 1.78 cm^{-1} Gpa^{-1}, respectively. The observable 29.8 Gpa of inflection point from the pressure-dependent Raman shift can provide robust evidence for the occurrence of the electronic topological transition (ETT), which widely exists in some representative metallic compounds (e.g., Sb_2S_3, Sb_2Se_3, Sb_2Te_3, Bi_2S_3, Bi_2Se_3, Bi_2Te_3, Ag_2Te, $AgBiSe_2$, etc.).[16,20−22,40−43] From Ahmad et al. (2020), no variations in volume and the Wyckoff positions of atoms were observed using synchrotron XRD during the occurrence of the ETT for $CrCl_3$.[17] However, the ETT is typical of a second-order IPT, which can be effectively determined using Raman spectroscopy based on the discontinuities in the pressure-dependent Raman shift and Raman fwhm.[20,22,41,42] Consequently, we made a detailed analysis of the Raman fwhm and spacings in the Raman shift versus pressure for $CrCl_3$, as illustrated in Figures 3 and 4a. The corresponding linear fitting results for the pressure-dependent Raman fwhm and spacings in the Raman shift are presented in Tables S2 and S3, respectively. It makes clear that the Raman peak intensity of $CrCl_3$ weakened progressively, accompanying the pronounced broadening in the Raman peaks with increasing pressure, particularly beyond 29.8 Gpa. Furthermore, two remarkable inflection points at 9.9 and 29.8 Gpa were found, which further verifies the occurrences of the IPT and ETT in $CrCl_3$. In short, all of these abovementioned clues, including the disappearance of the A_{g3} Raman peak, the notable discontinuities in the pressure-dependent Raman shift, Raman fwhm, and spacings in the Raman shift, provide sufficient evidence for the presence of the IPT and ETT in $CrCl_3$ at 9.9 and 29.8 GPa, respectively.

Upon decompression, all of the Raman peaks for $CrCl_3$ exhibited continuous redshifts, and no evident discontinuity was found in the pressure dependence of the Raman shift within the pressure range of 36.8−2.1 GPa. As the pressure was released to 1.8 GPa, the A_{g3} Raman peak emerged as denoted by an asterisk in Figure 5b. Upon further decompression to 0.8 GPa, all of the Raman peaks for $CrCl_3$ returned to their initial positions, indicating that the IPT is reversible. In addition, the

https://doi.org/10.1021/acs.inorgchem.1c03486
Inorg. Chem. 2022, 61, 4852−4864

evident discontinuities in the pressure-dependent Raman shift and spacings in the Raman shift at 1.8 GPa further confirmed the reversibility of the IPT. However, there existed a considerable pressure hysteresis for the IPT, which is probably correlated with the greater kinetic barrier upon decompression.

The high-pressure Raman spectra of $CrCl_3$ under hydrostatic conditions and the corresponding evolution of the Raman shift, Raman fwhm, and spacings in the Raman shift against pressure are depicted in detail in Figures S1, S2, and 4b, respectively. Experimental results manifested that the IPT and ETT of $CrCl_3$ occurred at higher pressure points of 11.7 and 32.2 GPa compared with those under nonhydrostatic conditions. Besides, upon decompression, the pressure dependence of the Raman shift and spacings in the Raman shift have similar variation tendencies with those under nonhydrostatic conditions, and a comparable phase transition pressure point of 2.6 GPa was obtained. The discrepancy in the phase transition pressure points for $CrCl_3$ under different hydrostatic environments can be reasonably explained by the deviatoric stress. In the case of the absence of the pressure medium, larger deviatoric stress exists in the sample chamber of the DAC, which promotes the occurrence of phase transition. By contrast, when the pressure medium is applied, the pressure hysteresis of phase transition probably origins from the protective effect of helium, which enters the interlayer space of $CrCl_3$ and thus reduces the deviatoric stress. Actually, a similar phenomenon of distinct phase transformation pressure points under different hydrostatic environments has also been reported in our previous investigations on other layered metallic compounds (e.g., MoS_2, $MoSe_2$, $MoTe_2$, ReS_2, As_2Te_3, etc.).[4,6,8,10,13]

3.2. High-Pressure Electrical Conductivity Results. A series of complex impedance spectra for $CrCl_3$ measured under conditions of 1.7−44.5 GPa and room temperature are illustrated in Figure 6. Within the pressure region of 1.7−29.7 GPa, the complex impedance spectra in the first quadrant were comprised of two parts: a high-frequency semicircle standing for the grain interior contribution of $CrCl_3$ and a low-frequency oblique line associating with the grain boundary contribution. We designed an equivalent circuit consisting of a resistance (R) and a constant phase element (CPE) in parallel to fit each impedance semicircular arc with Zview software. As the pressure reached 31.2 GPa, an oblique line representing the grain interior of $CrCl_3$, located in the fourth quadrant, and a simple resistance (R) was adopted to fit it. We calculated the electrical conductivity of $CrCl_3$ using the equation

$$\sigma = L/SR \quad (1)$$

where S and L represent the cross-sectional area of the electrode (cm^2) and the distance between electrodes (cm), and R and σ are the resistance (Ω) and the electrical conductivity (S/cm) of $CrCl_3$, respectively. Figure 7 plots the logarithmic electrical conductivity of $CrCl_3$ as a function of pressure upon both compression and decompression. Based on diverse pressure-dependent electrical conductivity slopes, three pressure regimes were distinguished: 1.7−10.3, 11.3−29.7, and 31.2−44.5 GPa. Within the pressure range of 1.7−10.3 GPa, an obvious enhancement in electrical conductivity at a rate of 0.063 S cm^{-1} GPa^{-1} was detected. However, the electrical conductivity of $CrCl_3$ remained relatively stable with a speed of 0.010 S cm^{-1} GPa^{-1} between 11.3 and 29.7 GPa. The remarkable inflection point in electrical conductivity at 10.3 GPa agrees well with our Raman scattering results and can be attributed to the IPT. Noteworthily, when the pressure was enhanced up to 31.2 GPa,

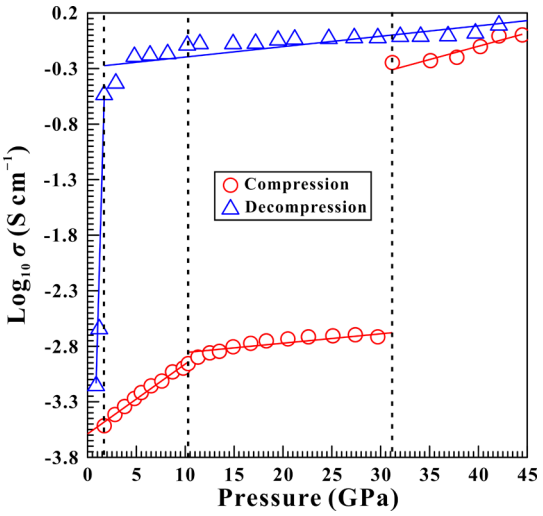

Figure 7. Variation of the logarithm of electrical conductivity along with the pressure in $CrCl_3$ during both processes of compression and decompression within the pressure ranges from 1.7 to 44.5 GPa.

the electrical conductivity of $CrCl_3$ raised steeply by about 3 orders of magnitude and then rose gently from 0.40 to 1.38 S/cm in the pressure range of 31.2−44.5 GPa. In fact, our previous high-pressure electrical conductivity studies have already disclosed that the noticeable jump in electrical conductivity is a typical characteristic of the semiconductor-to-metal transition.[44−46] Besides, above 31.2 GPa, the feeble electrical conductivity dependence relation with pressure provides another credible proof of metallization. Furthermore, the pressure point of metallization accords with that of the ETT, and thus, it is reasonable to speculate that the ETT may be accompanied by the metallization of $CrCl_3$. Upon decompression, a smooth decrease in electrical conductivity with a speed of 0.009 S cm^{-1} GPa^{-1} was obtained from 42.1 to 1.7 GPa. After being quenched down to 0.9 GPa, the electrical conductivity of $CrCl_3$ reverted to its original order of magnitude, implying that the metallization is reversible upon decompression.

3.3. Temperature-Dependent Electrical Conductivity Results. To confirm whether $CrCl_3$ underwent a metallization transition, we carried out temperature-dependent electrical conductivity measurements at some predesigned pressure points of 21.0, 28.5, 30.2, 31.8, and 33.1 GPa upon compression. Based on classical solid-state physics, the electrical conductivity of a semiconductor increases with the rise of temperature due to the thermally activated charge carriers. On the contrary, a negative relationship between the electrical conductivity and temperature is detected for metal owing to the enhancement of electron-phonon scattering.[4,15,25] Therefore, we can make an effective distinction between a semiconductor and metal through temperature-dependent electrical conductivity experiments. Below 30.2 GPa, the positive temperature-dependent electrical conductivity relations reflect that $CrCl_3$ is of semiconducting property (Figure 8a). As the pressure reached 31.8 GPa, the electrical conductivity decreased with increasing temperature, indicating that $CrCl_3$ underwent a metallization transition (Figure 8c). At the same time, we also measured the temperature dependence of electrical conductivity for $CrCl_3$ during the process of decompression at several representative pressure points of 23.1, 11.5, 3.9, 2.1, and 1.3 GPa to illustrate the metal-to-semiconductor transformation and accurately determine the

https://doi.org/10.1021/acs.inorgchem.1c03486
Inorg. Chem. 2022, 61, 4852−4864

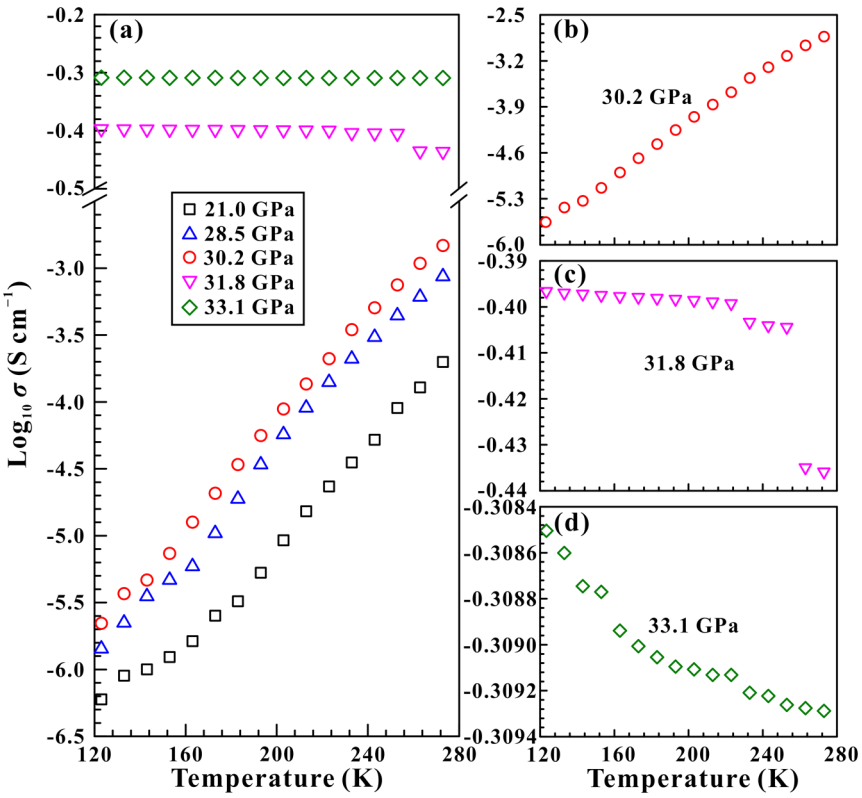

Figure 8. A series of variable-temperature electrical conductivity experiments for $CrCl_3$ at some predesigned pressure points. Here, (a) denotes all of these results at pressures of 21.0, 28.5, 30.2, 31.8, and 33.1 GPa upon compression; (b) denotes a typical semiconducting property of $CrCl_3$ at 30.2 GPa; (c) denotes the metallic behavior of the sample at 31.8 GPa and (d) denotes the metallic state for the sample at 33.1 GPa, respectively.

transition pressure point. Above 3.9 GPa, the sample exhibits a typical metallic behavior (Figure 9a). Obviously, a positive temperature-dependent electrical conductivity relation is observed as the pressure was released to 2.1 GPa, which is a representative feature of semiconductors (Figure 9c). In brief, our temperature-dependent electrical conductivity experiments provide robust evidence that semiconducting $CrCl_3$ transformed into a metallic state at 31.8 GPa upon compression, and the metallic $CrCl_3$ reverts to the initial semiconducting state at 2.1 GPa upon decompression. However, our obtained semiconductor-to-metal phase transition result for $CrCl_3$ is at variance with the semiconductor-to-semiconductor phase transition result previously reported by Ahmad et al. (2020).[17]

3.4. HRTEM Results. To thoroughly explore the microscopic crystalline structure of the samples, we performed HRTEM analyses on the starting and recovered samples decompressed from 39.4 GPa under nonhydrostatic conditions and decompressed from 39.7 GPa under hydrostatic conditions. As shown in Figure 10a,c, the initial and recovered samples under hydrostatic conditions possessed well-resolved and distinct lattice fringes with similar interplanar spacing values of 0.51 and 0.50 nm, which correspond to the (020) crystallographic plane of the monoclinic structure of $CrCl_3$. However, a smaller interplanar spacing value of 0.47 nm was acquired for the recovered sample under nonhydrostatic conditions (Figure 10b). Additionally, the corresponding fast Fourier transform (FFT) patterns of the HRTEM images provide more crystalline structural information for the starting and recovered samples, as illustrated in Figure 10d–f in detail. All of these acquired FFT patterns were composed of a series of diffraction spots, indicating the single-crystalline nature of the samples. As shown in Figures 10d,f, clear and defined diffraction spots were observed, suggesting that the initial and recovered samples under hydrostatic conditions have a high crystalline quality. However, the diffraction spots were relatively blurry and weak, indicating the low crystalline quality for the recovered sample under nonhydrostatic conditions (Figure 10e). The well-preserved crystalline structure for the recovered sample under hydrostatic conditions can be ascribed to the protective effect of the pressure medium. Under hydrostatic conditions, the smaller helium molecule with a diameter of approximately 0.26 nm may permeate the interlayer of $CrCl_3$ and thus relieve the interlayer interaction induced by compression, leading to the well-preserved interplanar spacing and crystallinity for the recovered sample. By contrast, without the protection of the pressure medium, the interplanar spacing will slightly reduce, and its crystallinity will be destroyed feebly for the recovered sample under nonhydrostatic conditions. Besides, the similar interplanar spacing values and the FFT patterns for the starting and recovered samples indicate that the pressure-induced phase transition in $CrCl_3$ is well reversible under different hydrostatic environments.

3.5. First-Principles Theoretical Calculations of $CrCl_3$. In order to further disclose either first- or second-order phase transition for $CrCl_3$ at the pressure of 30−35 GPa, the first-principles theoretical calculations of $CrCl_3$ were performed at a wide pressure range of 0−50.0 GPa, as shown in Figure 11. Some crucial parameters characteristic of the crystalline constants, including the enthalpy, unit cell volume, lattice constants (a, b, and c), angles (α, β, and γ), lattice constant ratio (a/c, a/b, and b/c), and normalized lattice constants (a/a_0, b/b_0, and c/c_0) for the antiferromagnetic and metallic phases, were successfully

https://doi.org/10.1021/acs.inorgchem.1c03486
Inorg. Chem. 2022, 61, 4852−4864

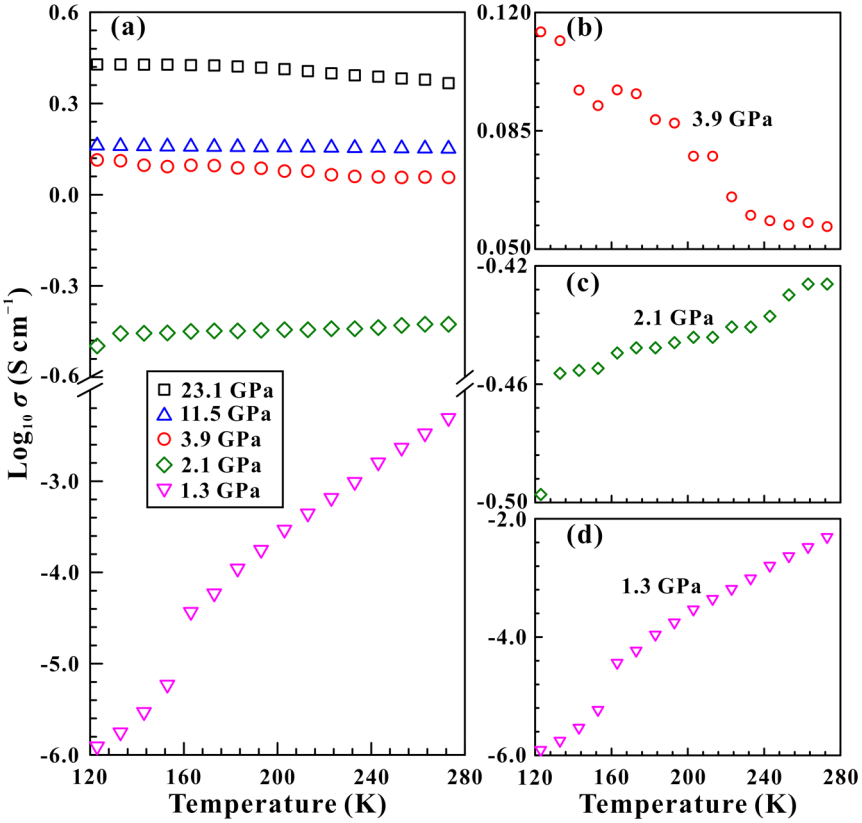

Figure 9. The temperature dependence of electrical conductivity measurements for $CrCl_3$ at some given pressure points. Here, (a) denotes all of these results at pressures of 23.1, 11.5, 3.9, 2.1, and 1.3 GPa upon decompression; (b) denotes a representative metallic property of the sample at 3.9 GPa; (c) denotes the semiconducting feature of the sample at 2.1 GPa and (d) denotes the semiconducting state for the sample at 1.3 GPa, respectively.

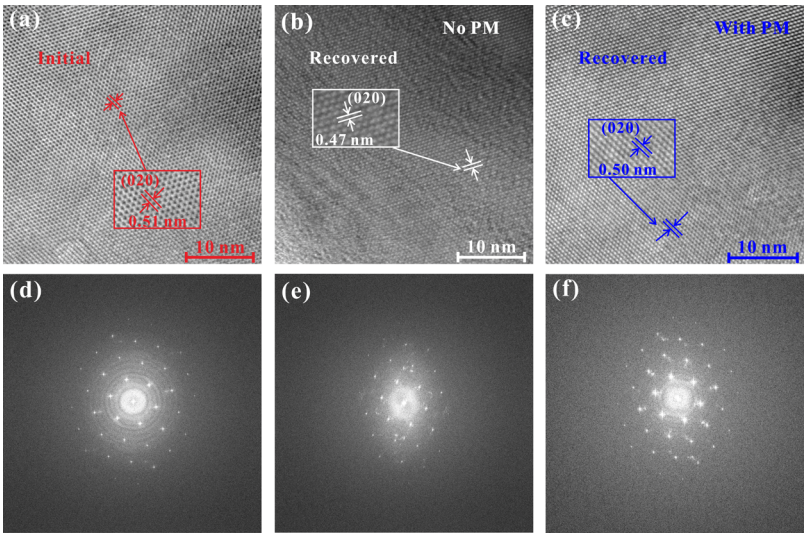

Figure 10. High-resolution transmission electron microscopy (HRTEM) images and their corresponding fast Fourier transform (FFT) patterns for $CrCl_3$. Here, (a,d) images of the initial sample; (b,e) images for the recovered sample decompressed from 39.4 GPa under nonhydrostatic conditions; (c,f) images for the recovered sample decompressed from 39.7 GPa under hydrostatic condition. The signal of PM stands for the pressure medium.

acquired, accordingly. As shown in Figure 11a–f, the calculated results make it clear that a huge volume reduction (or volume compression), and the obvious discontinuities in the pressure-dependent lattice constants (a and c), angle (β), lattice constant ratio (a/c, a/b, and b/c), and normalized lattice constants (a/a_0, b/b_0, and c/c_0) at the pressure range of 31.9–34.7 GPa, well proved the occurrence of metallization of $CrCl_3$. In addition, it is also evident that the metallization phase transformation in $CrCl_3$ at the pressure range of 31.9–34.7 GPa is possibly belonging to a typical first-order phase transition owing to the huge reduction of the unit cell volume. However, the variation of the unit cell volume is not obvious in previously reported synchrotron XRD results from Ahmad et al. (2020), which is possibly related to only limited high-pressure experimental measurements beyond 35.0 GPa.[17] In the other words, the metallic phase of $CrCl_3$ will be stabilized at only extremely high pressure above ~32.0 GPa.

https://doi.org/10.1021/acs.inorgchem.1c03486
Inorg. Chem. 2022, 61, 4852–4864

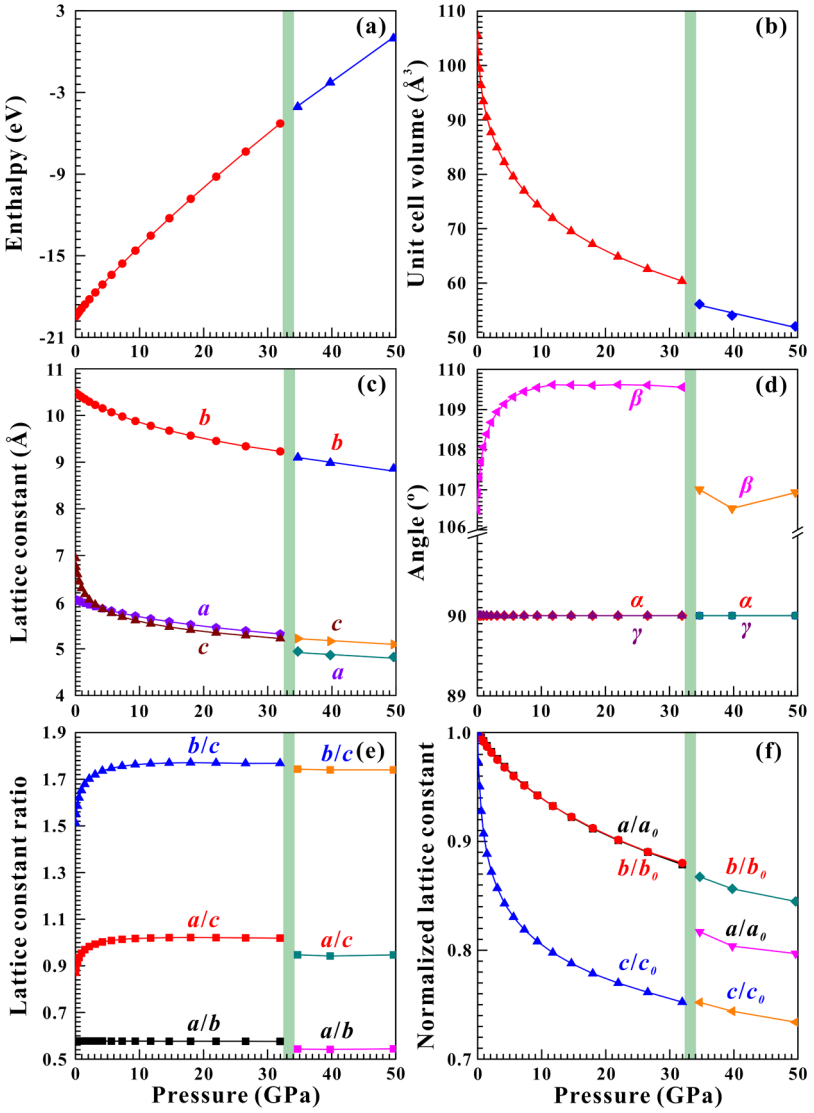

Figure 11. Calculated (a) enthalpy, (b) unit cell volume, (c) lattice constant, (d) angle, (e) lattice constant ratio, and (f) normalized lattice constant as a function of pressure for the antiferromagnetic and metallic $CrCl_3$ within the pressure range of 0−50.0 GPa. The calculated results make clear that a huge volume reduction (or volume compression), and the obvious discontinuities in the pressure-dependent lattice constants (a and b), angle (β), lattice constant ratio (a/c, a/b, and b/c), and normalized lattice constants (a/a_0, b/b_0, and c/c_0) at the pressure range of 31.9−34.7 GPa, well proved a typical first-order metallization phase transition in $CrCl_3$.

Before the phase transition occurs in $CrCl_3$, our calculated normalized lattice constant (a/a_0) is approximately 0.9 at the pressure of 30.0 GPa, which is in good agreement with the previously acquired results by Ahmad et al. (2020) from the high-pressure synchrotron XRD. After the phase transition in the sample is completed, our calculated normalized lattice constant (a/a_0) is approximately 0.8 at 35.0 GPa. In comparison with the previous high-pressure synchrotron XRD from Ahmad et al. (2020), we found that only one data point is illustrated in their experimental results, and thus, it is difficult to precisely determine the lattice parameters of $CrCl_3$ after the phase transition from their high-pressure synchrotron XRD results. In order to thoroughly resolve this issue, more detailed research work from the synchrotron XRD on $CrCl_3$ is indispensable under much higher pressure than 35.0 GPa.

At the same time, a series of calculated parameters characteristic of the electronic structures were also obtained for $CrCl_3$ under high pressure. In three representative pressure points of 0, 17.9, and 34.7 GPa, the variations of the observed magnitude of the band gap energy and its corresponding DOS are illustrated in Figure 12in detail. At atmospheric pressure, the 1.44 eV of the band gap energy in $CrCl_3$ is obtained, which is very close to previous results from the theoretically calculated value of 1.37 eV reported by Ahmad et al. (2020) at zero pressure.[17] When the pressure was increased up to 34.7 GPa, the band gap energy of $CrCl_3$ is gradually decreased to zero, and thus, the metallization of $CrCl_3$ appears at the pressure ranges from 17.9 to 34.7 GPa. In brief, the presently available metallization phase transition results of $CrCl_3$ based on the first-principles theoretical calculations are well consistent with our abovementioned electrical conductivity experiments under non-hydrostatic conditions.

In addition, in order to reveal the possible existence of the pressure-induced strong correlation behavior of chromium electrons, we also calculated the detailed electronic band structures of $CrCl_3$ by the first-principles theoretical calculations under conditions of two different U values (U = 0.0 eV and U = 3.0 eV), which corresponds to a critical pressure point of 34.7

https://doi.org/10.1021/acs.inorgchem.1c03486
Inorg. Chem. 2022, 61, 4852−4864

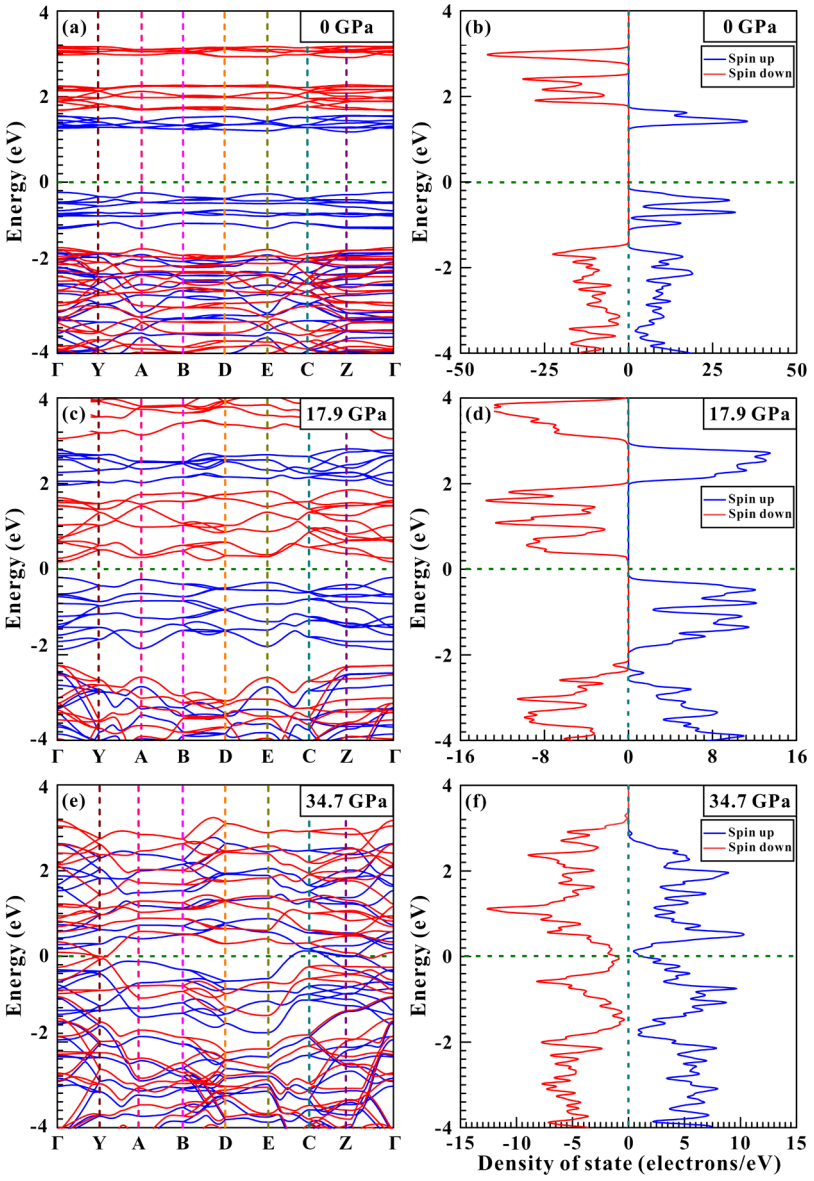

Figure 12. Calculated electronic band structures (a,c,e) and their corresponding density of states (b,d,f) for $CrCl_3$ at three representative pressure points of 0, 17.9, and 34.7 GPa, respectively. Here, the Fermi level is also shown as a green dashed line.

GPa before and after the occurrence of phase transformation from the semiconductor-to-metal phase.[30,31] We found that there is no obvious difference under two different controlled U values (3.0 eV) of the Hubbard-type correction. At a fixed pressure of 34.7 GPa, the band gap energy of $CrCl_3$ is zero at the condition of two different U values, as shown in Figure S4 in the Supporting Information.

4. CONCLUSIONS

We comprehensively explored the structural, vibrational, and electrical transport properties of $CrCl_3$ under different hydrostatic environments up to 50.0 GPa by Raman spectroscopy, AC impedance spectroscopy, HRTEM, and first-principles theoretical calculations. Under nonhydrostatic conditions, $CrCl_3$ underwent an IPT at 9.9 GPa followed by an ETT at 29.8 GPa. Furthermore, the ETT was accompanied by a metallization transformation, which was well confirmed by our variable-temperature electrical conductivity experiments and first-principles theoretical calculations. However, the phase transition pressure points of the IPT and ETT were delayed by about 2.0 GPa under hydrostatic conditions owing to the protection by the pressure medium. Upon decompression, the metallization of $CrCl_3$ was found to be reversible, which was proved by HRTEM results.

■ ASSOCIATED CONTENT

Supporting Information

The Supporting Information is available free of charge at https://pubs.acs.org/doi/10.1021/acs.inorgchem.1c03486.

High-pressure Raman spectra of $CrCl_3$ under hydrostatic conditions and their corresponding pressure-dependent Raman shift, Raman fwhm, and spacings in the Raman shift during the processes of compression and decompression, calculated electronic band structures of metallic $CrCl_3$ at different Hubbard U values (U = 0.0 eV and U = 3.0 eV) and at a fixed pressure of 34.7 GPa, and linear fitting results of the pressure-dependent Raman shift, Raman fwhm, and spacings in the Raman shift for $CrCl_3$

https://doi.org/10.1021/acs.inorgchem.1c03486
Inorg. Chem. 2022, 61, 4852−4864

under different hydrostatic environments during compression (PDF)

Accession Codes

CCDC 2151298 contains the supplementary crystallographic data for this paper. These data can be obtained free of charge via www.ccdc.cam.ac.uk/data_request/cif, or by emailing data_request@ccdc.cam.ac.uk, or by contacting The Cambridge Crystallographic Data Centre, 12 Union Road, Cambridge CB2 1EZ, UK; fax: +44 1223 336033.

AUTHOR INFORMATION

Corresponding Authors

Lidong Dai − *Key Laboratory of High-Temperature and High-Pressure Study of the Earth's Interior, Institute of Geochemistry, Chinese Academy of Sciences, Guizhou 550081, China*; orcid.org/0000-0002-9081-765X; Email: dailidong@vip.gyig.ac.cn

Haiying Hu − *Key Laboratory of High-Temperature and High-Pressure Study of the Earth's Interior, Institute of Geochemistry, Chinese Academy of Sciences, Guizhou 550081, China*; Email: huhaiying@vip.gyig.ac.cn

Authors

Meiling Hong − *Key Laboratory of High-Temperature and High-Pressure Study of the Earth's Interior, Institute of Geochemistry, Chinese Academy of Sciences, Guizhou 550081, China; University of Chinese Academy of Sciences, Beijing 100049, China*

Xinyu Zhang − *Key Laboratory of High-Temperature and High-Pressure Study of the Earth's Interior, Institute of Geochemistry, Chinese Academy of Sciences, Guizhou 550081, China; University of Chinese Academy of Sciences, Beijing 100049, China*

Chuang Li − *Key Laboratory of High-Temperature and High-Pressure Study of the Earth's Interior, Institute of Geochemistry, Chinese Academy of Sciences, Guizhou 550081, China; University of Chinese Academy of Sciences, Beijing 100049, China*

Yu He − *Key Laboratory of High-Temperature and High-Pressure Study of the Earth's Interior, Institute of Geochemistry, Chinese Academy of Sciences, Guizhou 550081, China; University of Chinese Academy of Sciences, Beijing 100049, China*; orcid.org/0000-0001-6518-585X

Complete contact information is available at: https://pubs.acs.org/10.1021/acs.inorgchem.1c03486

Author Contributions

L.D. and H.H. conceived the idea and led the project. M.H., X.Z., and C.L. designed the experiments and performed the X-ray diffraction, high-pressure Raman spectra, high-pressure electrical conductivity, and high-resolution transmission electron microscopy measurements. Y.H. performed the first-principles theoretical calculations. L.D. and M.H. contributed to the analysis, interpretation, and discussion of results. M.H. wrote the manuscript with the help of all the authors. All the authors commented on the final manuscript. L.D. and H.H. supervised the project.

Notes

The authors declare no competing financial interest.

ACKNOWLEDGMENTS

The authors thank the editor, Professor Hiroshi Kageyama, and four anonymous reviewers for their very constructive and enlightened comments and suggestions in the reviewing process, which helped us greatly in improving the manuscript. The authors acknowledge the technical support of the in situ high-pressure Raman scattering measurements provided by Professor Heping Li at the Key Laboratory of High-temperature and High-pressure Study of the Earth's Interior, Institute of Geochemistry, Chinese Academy of Sciences. This research was funded by the NSF of China (grant numbers 42072055, 41774099, 41772042, and 42074104), the Youth Innovation Promotion Association of CAS (grant number 2019390), and the Special Fund of the West Light Foundation of CAS. Numerical computations were performed at the Hefei advanced computing center.

REFERENCES

(1) Craco, L.; Carara, S. S.; Shao, Y.-C.; Chuang, Y.-D.; Freelon, B. Electronic structure of rhombohedral CrX3 (X=Br, Cl, I) van der Waals crystals. *Phys. Rev. B* **2021**, *103*, 235119.

(2) Kazim, S.; Alì, M.; Palleschi, S.; D'Olimpio, G.; Mastrippolito, D.; Politano, A.; Gunnella, R.; Di Cicco, A.; Renzelli, M.; Moccia, G.; Cacioppo, O. A.; Alfonsetti, R.; Strychalska-Nowak, J.; Klimczuk, T.; J Cava, R.; Ottaviano, L. Mechanical exfoliation and layer number identification of single crystal monoclinic CrCl3. *Nanotechnology* **2020**, *31*, 395706.

(3) Mastrippolito, D.; Ottaviano, L.; Wang, J.; Yang, J.; Gao, F.; Ali, M.; D'Olimpio, G.; Politano, A.; Palleschi, S.; Kazim, S.; Gunnella, R.; Di Cicco, A.; Sgarlata, A.; Strychalska-Nowak, J.; Klimczuk, T.; Cava, R. J.; Lozzi, L.; Profeta, G. Emerging oxidized and defective phases in low-dimensional CrCl3. *Nanoscale Adv.* **2021**, *3*, 4756−4766.

(4) Zhuang, Y.; Dai, L.; Wu, L.; Li, H.; Hu, H.; Liu, K.; Yang, L.; Pu, C. Pressure-induced permanent metallization with reversible structural transition in molybdenum disulfide. *Appl. Phys. Lett.* **2017**, *110*, 122103.

(5) Nayak, A. P.; Pandey, T.; Voiry, D.; Liu, J.; Moran, S. T.; Sharma, A.; Tan, C.; Chen, C.-H.; Li, L.-J.; Chhowalla, M.; Lin, J.-F.; Singh, A. K.; Akinwande, D. Pressure-dependent optical and vibrational properties of monolayer molybdenum disulfide. *Nano Lett.* **2015**, *15*, 346−353.

(6) Yang, L.; Dai, L.; Li, H.; Hu, H.; Liu, K.; Pu, C.; Hong, M.; Liu, P. Pressure-induced metallization in MoSe2 under different pressure conditions. *RSC Adv.* **2019**, *9*, 5794−5803.

(7) Rifliková, M.; Martoňák, R.; Tosatti, E. Pressure-induced gap closing and metallization of $MoSe_2$ and $MoTe_2$. *Phys. Rev. B: Condens. Matter Mater. Phys.* **2014**, *90*, 035108.

(8) Yang, L.; Dai, L.; Li, H.; Hu, H.; Liu, K.; Pu, C.; Hong, M.; Liu, P. Characterization of the pressure-induced phase transition of metallization for MoTe2 under hydrostatic and non-hydrostatic conditions. *AIP Adv.* **2019**, *9*, 065104.

(9) Bera, A.; Singh, A.; Muthu, D. V. S.; Waghmare, U. V.; Sood, A. K. Pressure-dependent semiconductor to semimetal and Lifshitz transitions in 2H-MoTe2: Raman and first-principles studies. *J. Phys.: Condens. Matter* **2017**, *29*, 105403.

(10) Zhuang, Y.; Dai, L.; Li, H.; Hu, H.; Liu, K.; Yang, L.; Pu, C.; Hong, M.; Liu, P. Deviatoric stresses promoted metallization in rhenium disulfide. *J. Phys. D: Appl. Phys.* **2018**, *51*, 165101.

(11) Saha, P.; Ghosh, B.; Mazumder, A.; Glazyrin, K.; Dev Mukherjee, G. Pressure induced lattice expansion and phonon softening in layered ReS2. *J. Appl. Phys.* **2020**, *128*, 085904.

(12) Liu, K.; Dai, L.; Li, H.; Hu, H.; Yang, L.; Pu, C.; Hong, M.; Liu, P. Phase transition and metallization of orpiment by Raman spectroscopy, electrical conductivity and theoretical calculation under high pressure. *Materials* **2019**, *12*, 784.

(13) Dai, L.; Zhuang, Y.; Li, H.; Wu, L.; Hu, H.; Liu, K.; Yang, L.; Pu, C. Pressure-induced irreversible amorphization and metallization with a structural phase transition in arsenic telluride. *J. Mater. Chem. C* **2017**, *5*, 12157−12162.

(14) Cuenca-Gotor, V. P.; Sans, J. A.; Ibáñez, J.; Popescu, C.; Gomis, O.; Vilaplana, R.; Manjón, F. J.; Leonardo, A.; Sagasta, E.; Suárez-Alcubilla, A.; Gurtubay, I. G.; Mollar, M.; Bergara, A. Structural, Vibrational, and Electronic Study of α-As2Te3 under Compression. *J. Phys. Chem. C* **2016**, *120*, 19340−19352.
(15) Dai, L.; Liu, K.; Li, H.; Wu, L.; Hu, H.; Zhuang, Y.; Yang, L.; Pu, C.; Liu, P. Pressure-induced irreversible metallization accompanying the phase transitions in Sb_2S_3. *Phys. Rev. B* **2018**, *97*, 024103.
(16) Ibáñez, J.; Sans, J. A.; Popescu, C.; López-Vidrier, J.; Elvira-Betanzos, J. J.; Cuenca-Gotor, V. P.; Gomis, O.; Manjón, F. J.; Rodríguez-Hernández, P.; Muñoz, A. Structural, vibrational, and electronic study of Sb_2S_3 at high pressure. *J. Phys. Chem. C* **2016**, *120*, 10547−10558.
(17) Ahmad, A. S.; Liang, Y.; Dong, M.; Zhou, X.; Fang, L.; Xia, Y.; Dai, J.; Yan, X.; Yu, X.; Dai, J.; Zhang, G.-j.; Zhang, W.; Zhao, Y.; Wang, S. Pressure-driven switching of magnetism in layered CrCl3. *Nanoscale* **2020**, *12*, 22935−22944.
(18) Chen, X.; Lou, H.; Zeng, Z.; Cheng, B.; Zhang, X.; Liu, Y.; Xu, D.; Yang, K.; Zeng, Q. Structural transitions of 4:1 methanol-ethanol mixture and silicone oil under high pressure. *Matter Radiat. Extremes* **2021**, *6*, 038402.
(19) Klotz, S.; Chervin, J.-C.; Munsch, P.; Le Marchand, G. Hydrostatic limits of 11 pressure transmitting media. *J. Phys. D: Appl. Phys.* **2009**, *42*, 075413.
(20) Bera, A.; Pal, K.; Muthu, D. V. S.; Sen, S.; Guptasarma, P.; Waghmare, U. V.; Sood, A. K. Sharp Raman Anomalies and Broken Adiabaticity at a Pressure Induced Transition from Band to Topological Insulator inSb2Se3. *Phys. Rev. Lett.* **2013**, *110*, 107401.
(21) Gomis, O.; Vilaplana, R.; Manjón, F. J.; Rodríguez-Hernández, P.; Pérez-González, E.; Muñoz, A.; Kucek, V.; Drasar, C. Lattice dynamics of Sb2Te3at high pressures. *Phys. Rev. B: Condens. Matter Mater. Phys.* **2011**, *84*, 174305.
(22) Rajaji, V.; Malavi, P. S.; Yamijala, S. S. R. K. C.; Sorb, Y. A.; Dutta, U.; Guin, S. N.; Joseph, B.; Pati, S. K.; Karmakar, S.; Biswas, K.; Narayana, C. Pressure induced structural, electronic topological, and semiconductor to metal transition in AgBiSe2. *Appl. Phys. Lett.* **2016**, *109*, 171903.
(23) Vilaplana, R.; Sans, J. A.; Manjón, F. J.; Andrada-Chacón, A.; Sánchez-Benítez, J.; Popescu, C.; Gomis, O.; Pereira, A. L. J.; García-Domene, B.; Rodríguez-Hernández, P.; Muñoz, A.; Daisenberger, D.; Oeckler, O. Structural and electrical study of the topological insulator SnBi2Te4 at high pressure. *J. Alloys Compd.* **2016**, *685*, 962−970.
(24) Morosin, B.; Narath, A. X-Ray Diffraction and Nuclear Quadrupole Resonance Studies of Chromium Trichloride. *J. Chem. Phys.* **1964**, *40*, 1958−1967.
(25) Yang, L.; Jiang, J.; Dai, L.; Hu, H.; Hong, M.; Zhang, X.; Li, H.; Liu, P. High-pressure structural phase transition and metallization in Ga2S3 under non-hydrostatic and hydrostatic conditions up to 36.4 GPa. *J. Mater. Chem. C* **2021**, *9*, 2912−2918.
(26) Kresse, G.; Furthmüller, J. Efficient iterative schemes forab initiototal-energy calculations using a plane-wave basis set. *Phys. Rev. B: Condens. Matter Mater. Phys.* **1996**, *54*, 11169−11186.
(27) Kresse, G.; Furthmüller, J. Efficiency of ab-initio total energy calculations for metals and semiconductors using a plane-wave basis set. *Comput. Mater. Sci.* **1996**, *6*, 15−50.
(28) Blöchl, P. E.; Jepsen, O.; Andersen, O. K. Improved tetrahedron method for Brillouin-zone integrations. *Phys. Rev. B: Condens. Matter Mater. Phys.* **1994**, *49*, 16223.
(29) Perdew, J. P.; Burke, K.; Ernzerhof, M. Generalized gradient approximation made simple. *Phys. Rev. Lett.* **1996**, *77*, 3865−3868.
(30) Bengone, O.; Alouani, M.; Blöchl, P.; Hugel, J. Implementation of the projector augmented-wave LDA+U method: Application to the electronic structure of NiO. *Phys. Rev. B: Condens. Matter Mater. Phys.* **2000**, *62*, 16392−16401.
(31) Liechtenstein, A. I.; Anisimov, V. I.; Zaanen, J. Density-functional theory and strong interactions: Orbital ordering in Mott-Hubbard insulators. *Phys. Rev. B: Condens. Matter Mater. Phys.* **1995**, *52*, R5467−R5470.
(32) He, Y.; Sun, S.; Kim, D. Y.; Jang, B. G.; Li, H.; Mao, H.-k. Superionic iron alloys and their seismic velocities in Earth's inner core. *Nature* **2022**, *602*, 258−262.
(33) Hou, M.; He, Y.; Jang, B. G.; Sun, S.; Zhuang, Y.; Deng, L.; Tang, R.; Chen, J.; Ke, F.; Meng, Y.; Prakapenka, V. B.; Chen, B.; Shim, J. H.; Liu, J.; Kim, D. Y.; Hu, Q.; Pickard, C. J.; Needs, R. J.; Mao, H.-K. Superionic iron oxide-hydroxide in Earth's deep mantle. *Nat. Geosci.* **2021**, *14*, 174−178.
(34) He, Y.; Dai, L.; Kim, D. Y.; Li, H. P.; Karato, S.-i. Thermal ionization of hydrogen in hydrous olivine with enhanced and anisotropic conductivity. *J. Geophys. Res. Solid Earth* **2021**, *126*, No. e2021JB022939.
(35) He, Y.; Sun, S.; Li, H. Ab initio molecular dynamics investigation of the elastic properties of superionic Li2O under high temperature and pressure. *Phys. Rev. B* **2021**, *103*, 174105.
(36) He, Y.; Lu, X.; Kim, D. Y. A first-principles study on Si24 as an anode material for rechargeable batteries. *RSC Adv.* **2018**, *8*, 20228−20233.
(37) Glamazda, A.; Lemmens, P.; Do, S.-H.; Kwon, Y. S.; Choi, K.-Y. Relation between Kitaev magnetism and structure in α−RuCl3. *Phys. Rev. B* **2017**, *95*, 174429.
(38) Cheng, Z.-P.; He, B.-G.; Li, H.; Zhang, W.-B. Effect of thickness and stacking order on Raman spectrum of layered $CrCl_3$. *J. Phys.: Condens. Matter* **2021**, *33*, 355401.
(39) Kanesaka, I.; Kawahara, H.; Yamazaki, A.; Kawai, K. The vibrational spectrum of MCl3 (M = Al, Cr and Fe). *J. Mol. Struct.* **1986**, *146*, 41−49.
(40) Yang, M.; Luo, Y. Z.; Zeng, M. G.; Shen, L.; Lu, Y. H.; Zhou, J.; Wang, S. J.; Sou, I. K.; Feng, Y. P. Pressure induced topological phase transition in layered Bi2S3. *Phys. Chem. Chem. Phys.* **2017**, *19*, 29372−29380.
(41) Vilaplana, R.; Santamaría-Pérez, D.; Gomis, O.; Manjón, F. J.; González, J.; Segura, A.; Muñoz, A.; Rodríguez-Hernández, P.; Pérez-González, E.; Marín-Borrás, V.; Muñoz-Sanjose, V.; Drasar, C.; Kucek, V. Structural and vibrational study of Bi2Se3under high pressure. *Phys. Rev. B: Condens. Matter Mater. Phys.* **2011**, *84*, 184110.
(42) Vilaplana, R.; Gomis, O.; Manjón, F. J.; Segura, A.; Pérez-González, E.; Rodríguez-Hernández, P.; Muñoz, A.; González, J.; Marín-Borrás, V.; Muñoz-Sanjosé, V.; Drasar, C.; Kucek, V. High-pressure vibrational and optical study of Bi2Te3. *Phys. Rev. B: Condens. Matter Mater. Phys.* **2011**, *84*, 104112.
(43) Zhang, Y.; Li, Y.; Ma, Y.; Li, Y.; Li, G.; Shao, X.; Wang, H.; Cui, T.; Wang, X.; Zhu, P. Electronic Topological Transition in Ag2Te at High-pressure. *Sci. Rep.* **2015**, *5*, 14681.
(44) Dai, L.; Pu, C.; Li, H.; Hu, H.; Liu, K.; Yang, L.; Hong, M. Characterization of metallization and amorphization for GaP under different hydrostatic environments in diamond anvil cell up to 40.0 GPa. *Rev. Sci. Instrum.* **2019**, *90*, 066103.
(45) Pu, C.; Dai, L.; Li, H.; Hu, H.; Liu, K.; Yang, L.; Hong, M. Pressure-induced phase transitions of ZnSe under different pressure environments. *AIP Adv.* **2019**, *9*, 025004.
(46) Hong, M.; Dai, L.; Li, H.; Hu, H.; Liu, K.; Yang, L.; Pu, C. Structural phase transition and metallization of nanocrystalline rutile investigated by high-pressure Raman spectroscopy and electrical conductivity. *Minerals* **2019**, *9*, 441.

https://doi.org/10.1021/acs.inorgchem.1c03486
Inorg. Chem. 2022, 61, 4852−4864